Research Article Vol. 13, No. 5 / May 2026 / Optica 977

OPTICA

Hyperentanglement-enabled noise-resilient quantum communication over a 40 km intra-city fiber network

HEEBONG SEO,[1,4] JIN-HUN KIM,[2] U-SHIN KIM,[1] SEUNG-YEUN YOO,[1] HEE SU PARK,[3] SANG MIN LEE,[3] YOUN-CHANG JEONG,[2,5] AND YOON-HO KIM[1,*]

[1] Department of Physics, Pohang University of Science and Technology (POSTECH), Pohang 37673, Republic of Korea
[2] The affiliated institute of ETRI, Daejeon 34044, Republic of Korea
[3] Korea Research Institute of Standards and Science, Daejeon 34113, Republic of Korea
[4] heebongseo@gmail.com
[5] w31400@gmail.com
*yoonho72@gmail.com

Received 12 August 2025; revised 20 April 2026; accepted 24 April 2026; published 19 May 2026

Entanglement distribution over deployed fiber links is essential for implementing quantum communication protocols. However, environmental noise in deployed fibers, such as classical signals, stray light, and Raman scattering, can significantly degrade entanglement, ultimately destroying the nonlocal correlations required for quantum communication. In this work, we demonstrate noise-resilient quantum communication over 40 km of intra-city deployed fiber, with a total transmission loss of 23.04 dB, by utilizing hyperentanglement in the time-bin and frequency degrees of freedom. By exploiting the frequency anticorrelation of the photon pairs and implementing frequency-to-time mapping using dense wavelength-division multiplexing combined with calibrated delay lines, we realize frequency-resolved detection that discriminates frequency-anticorrelated entangled photon pairs from uncorrelated noise. This enables reliable entanglement distribution with over an order-of-magnitude improvement in signal-to-noise ratio and a substantial increase in Bell-state fidelity, even in high-noise and high-loss conditions of deployed fibers. Moreover, entanglement—initially lost due to entanglement sudden death—is successfully restored, enabling a clear violation of the Bell inequality. These results establish a practical and scalable method for entanglement distribution in noisy and lossy environments, advancing the feasibility of real-world quantum communication over existing fiber infrastructure.

https://doi.org/10.1364/OPTICA.576289

1. INTRODUCTION

The realization of quantum communication protocols such as quantum key distribution (QKD) [1–7], quantum teleportation [8–14], quantum dense coding [15–19], and quantum networking [20,21] requires entanglement distribution between distant parties. While both fiber-optic links and free-space channels are viable platforms, recent efforts have increasingly focused on using existing deployed fiber infrastructure as a practical and cost-effective solution, where classical and quantum signals coexist [22–24]. However, real-world implementation faces major challenges: co-propagating classical signals, stray light, crosstalk, and spontaneous Raman scattering introduce substantial noise that can overwhelm weak quantum signals [22]. In addition, intrinsic transmission loss causes exponential signal decay, further reducing the signal-to-noise ratio (SNR) and degrading entanglement [25,26]. These issues have become bottlenecks for scalable and reliable quantum communication over deployed networks.

To address these limitations, various strategies have been explored, including high-dimensional quantum encoding [27–30] and wavelength filtering [22,31]. High-dimensional systems such as time-bin or orbital angular momentum modes offer increased information capacity and potential noise robustness. However, they often require complex state preparation and detection, and are generally incompatible with widely used qubit-based protocols [30,32]. Wavelength filtering attempts to spectrally separate quantum and classical signals but cannot fully eliminate overlapping noise spectra in deployed fibers [31].

In contrast, hyperentanglement, simultaneous entanglement in multiple degrees of freedom such as time-bin, polarization, frequency, and orbital angular momentum, provides a powerful resource for noise-resilient quantum communication [33–37]. One degree of freedom can be used to isolate quantum-correlated signals from noise, while the other retains entanglement for protocol operations, such as teleportation, dense coding, or key distribution [35]. By utilizing such quantum correlations as an active resource, this approach achieves noise rejection capabilities beyond conventional filtering, while maintaining compatibility with qubit-based protocols. Although hyperentanglement-based noise suppression has been proposed and demonstrated under controlled laboratory conditions [35], it has not yet been realized in real-world deployed fiber environments.

In this work, we report the first experimental demonstration of hyperentanglement-enabled entanglement distribution over a 40 km intra-city fiber network, with a total channel loss of 23.04 dB. By exploiting the frequency anticorrelation of hyperentangled photon pairs and implementing frequency-to-time mapping using dense wavelength-division multiplexing (DWDM) combined with calibrated delay lines, we realize frequency-resolved detection that discriminates frequency-anticorrelated photon pairs from uncorrelated noise. This enables reliable entanglement distribution with more than an order-of-magnitude improvement in SNR (from 0.84 to 12.10), a substantial increase in Bell-state fidelity (from 0.49 to 0.89), and restoration of entanglement that had been lost due to entanglement sudden death. Furthermore, we observe a clear violation of the Bell inequality by 3.53 standard deviations. Altogether, our results demonstrate a viable strategy for entanglement distribution under real-world noise and loss, paving the way for robust quantum communication over metropolitan-scale fiber networks.

2. EXPERIMENT

Consider the distribution of a time-bin entangled photon pair prepared in the Bell state

$$|\phi^{(+)}\rangle = \frac{1}{\sqrt{2}}(|EE\rangle + |LL\rangle), \tag{1}$$

where $|E\rangle$ and $|L\rangle$ denote the early and late time-bin modes, respectively [38,39]. Time-bin entanglement is particularly well suited for fiber-based quantum communication due to its robustness against polarization-mode dispersion. However, when propagating through deployed fibers, photons encounter substantial noise from sources such as stray light, co-propagating classical signals, and spontaneous Raman scattering. These noise contributions can be effectively modeled as a depolarizing channel [40,41], which captures the loss of coherence due to uncorrelated noise. Under this model, the transmitted time-bin state is described by the density matrix:

$$\rho_0 = (1-p)|\phi^{(+)}\rangle\langle\phi^{(+)}| + \frac{p}{4}\hat{\mathbb{I}}_{\text{tb}}, \tag{2}$$

where p $(0 \le p \le 1)$ represents the noise portion and $\hat{\mathbb{I}}_{\text{tb}}$ is the identity operator in the time-bin basis [42,43]. The first term corresponds to the signal component, while the second represents maximally mixed noise. This leads to the SNR of $2(1-p)/p$, which decreases as the noise portion p increases, ultimately degrading the entanglement of the photon pair transmitted through the depolarizing channel.

The degradation of entanglement under high noise severely limits its usefulness for quantum communication via deployed fibers. To overcome this problem, we exploit hyperentanglement in the time-bin and frequency degrees of freedom. By taking advantage of the strong frequency anticorrelation of the photon pair [44–47], we implement a frequency-resolved detection scheme that distinguishes entangled photons from uncorrelated noise. The frequency-resolving module maps different frequency components to distinct arrival times, enabling selective detection of frequency-anticorrelated pairs [48,49]. This approach effectively filters out uncorrelated noise and restores entanglement even in high-loss and high-noise conditions.

The hyperentangled state after transmission through the depolarizing channel is described by

$$\rho_1 = (1-p)|\phi^{(+)}\rangle\langle\phi^{(+)}| \otimes |\psi\rangle\langle\psi| + \frac{p}{4N^2}\hat{\mathbb{I}}_{\text{tb}} \otimes \hat{\mathbb{I}}_{\text{freq}}, \tag{3}$$

where $|\psi\rangle = \frac{1}{\sqrt{N}}\sum_{n_\text{A}=1}^{N}|n_\text{A}n_\text{B}\rangle$, with $n_\text{B} = N + 1 - n_\text{A}$, is the N-dimensional frequency-anticorrelated state. The basis state $|n_\text{A}n_\text{B}\rangle$ denotes the frequency modes of the photons sent to Alice and Bob, and $\hat{\mathbb{I}}_{\text{freq}}$ is the identity operator on the frequency subspace.

To isolate the frequency-anticorrelated entangled photons from the uncorrelated noise, we apply a frequency-resolving module that maps each frequency mode to a distinct temporal mode. This is achieved by discretizing the frequency domain into N bins and assigning a specific time delay to each via optical path differences [35]. As a result, frequency modes are converted into distinguishable arrival times, enabling selective detection of correlated photon pairs and effective suppression of uncorrelated noise. Figure 1(a) illustrates the joint spectral intensity of the hyperentangled photon pair overlaid with spectrally flat white noise induced by the depolarizing channel. The noise uniformly spans the full frequency range, while the entangled pairs are confined to the diagonal due to their anticorrelation. After isolating the anticorrelated modes via temporal filtering, the residual noise is significantly reduced, as shown in Fig. 1(b).

After the frequency-resolved detection, the resulting quantum state is given by the projection onto the frequency-anticorrelated modes:

$$\begin{aligned}\rho &= \mathcal{C}\sum_{n_\text{A}=1}^{N}\langle n_\text{A}n_\text{B}|\rho_1|n_\text{A}n_\text{B}\rangle \\ &= \mathcal{C}\left[(1-p)|\phi^{(+)}\rangle\langle\phi^{(+)}| + \frac{p}{4N}\hat{\mathbb{I}}_{\text{tb}}\right],\end{aligned} \tag{4}$$

where $\mathcal{C}$ is the normalization constant. Compared to Eq. (2), the noise term is reduced by a factor of $1/N$, reflecting the spectral filtering effect of the frequency-resolving module.

The resulting SNR is then

$$\begin{aligned}\text{SNR} &= \frac{(1-p)\sum_i^{EE,LL}\langle i|\phi^{(+)}\rangle\langle\phi^{(+)}|i\rangle}{(p/4N)\sum_i^{EE,LL}\langle i|\hat{\mathbb{I}}_{\text{tb}}|i\rangle} \\ &= \frac{2N(1-p)}{p}.\end{aligned} \tag{5}$$

This expression shows that the SNR increases linearly with N, enabling significant enhancement of entanglement robustness in high-noise and high-loss fiber environments through the use of hyperentanglement and frequency-resolved detection.

Figure 1(c) shows the conceptual schematic of hyperentanglement-enabled noise-resilient quantum communication over a 40 km intra-city fiber network. A photon pair hyperentangled in time-bin and frequency is generated using an unbalanced Michelson interferometer and spontaneous parametric down-conversion (SPDC). One photon is transmitted to Alice through a 20 km segment of deployed fiber connecting the National Security Research Institute (NSR) and the Korea Research Institute of Standards and Science (KRISS), via the

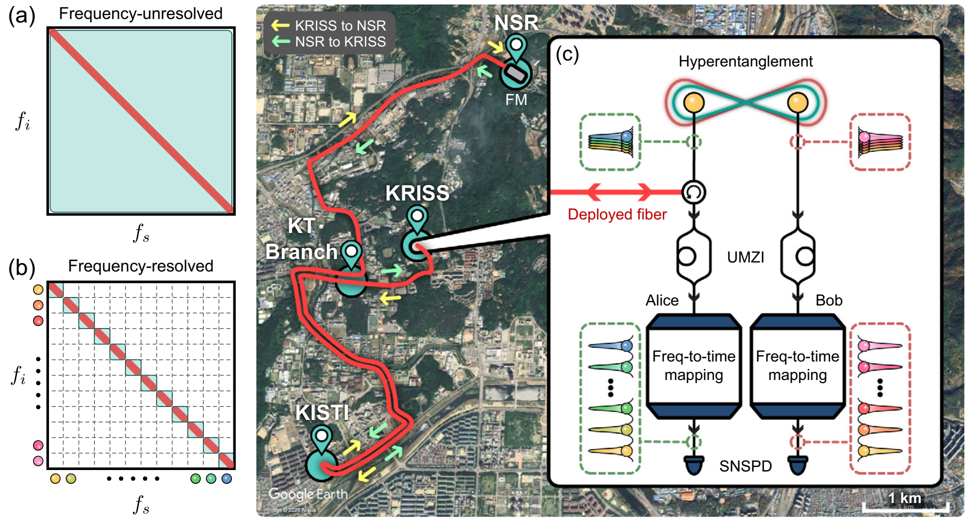

Fig. 1. Conceptual schematic of the experiment. (a) Joint spectral intensity (JSI) of an entangled photon pair, showing a frequency-anticorrelated distribution (red line), overlaid with uncorrelated white noise (blue region). (b) JSI after selecting the frequency-anticorrelated mode using the frequency-resolving module, which maps frequency components to distinct temporal modes. (c) a 40 km intra-city fiber network, connecting the National Security Research Institute (NSR) to the Korea Research Institute of Standards and Science (KRISS) in Daejeon, South Korea. The total transmission loss is 23.04 dB. FM, Faraday mirror; UMZI, unbalanced Mach–Zehnder Interferometer; and SNSPD, superconducting nanowire single-photon detector.

KT Buk-Daejeon branch and the Korea Institute of Science and Technology Information (KISTI) in Daejeon, South Korea. The photon is reflected at the end of the channel by a Faraday mirror (FM) and returns to Alice, resulting in a total propagation distance of 40 km with an overall fiber loss of 23.04 dB. The time-bin entangled photon pair is analyzed using unbalanced Mach–Zehnder interferometers (UMZIs) at Alice and Bob, while the frequency-resolving module maps photon frequencies to distinct arrival times, enabling temporal discrimination based on frequency.

Figure 2 shows the detailed experimental setup for hyperentanglement-enabled noise-resilient quantum communication over the 40 km fiber network. A picosecond pulsed laser (FPL-02CTT; Calmar Laser, pulse repetition rate of 18.02 MHz) centered at 1552.52 nm is first split into two pulses separated by 15 ns using an unbalanced Michelson interferometer (UMI), which is actively phase-stabilized via an auxiliary continuous-wave laser and a fiber phase shifter (FPS). The resulting pulses are frequency-doubled to 776.26 nm by second-harmonic generation (SHG) in a type-0 periodically poled lithium niobate (PPLN) crystal (length: 35 mm and poling period: 19.3 μm). These pulses then pump a type-0 PPLN waveguide (length: 20 mm and poling period: 17.0 μm), generating photon pairs via SPDC. The SPDC output has a 3 dB bandwidth of approximately 90 nm centered at 1552.52 nm.

The generated photon pair exhibits time-bin entanglement, arising from the indistinguishability of the pump pulse origin, and frequency entanglement, due to energy conservation in the SPDC process, resulting in strong frequency anticorrelation. In this work, time-bin modes are chosen for their robustness against polarization-mode dispersion [50], while frequency modes provide access to high-dimensional encoding [35]. The resulting

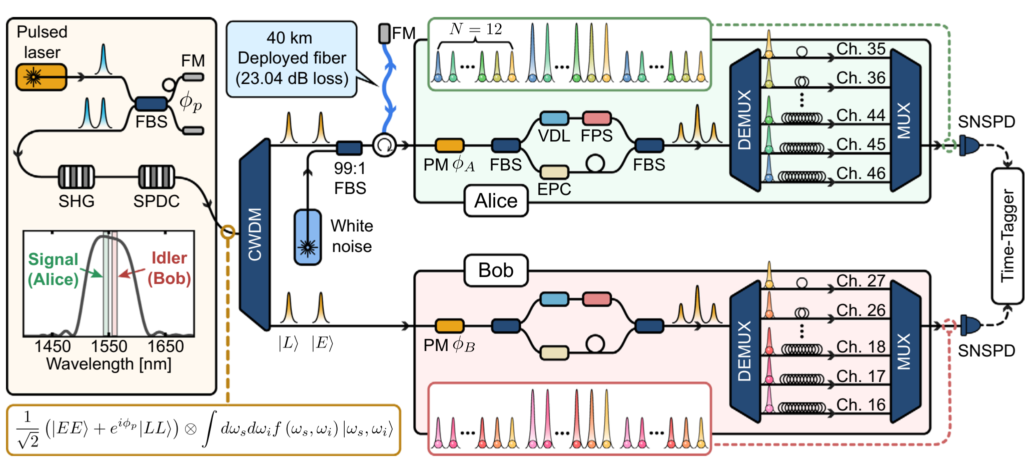

Fig. 2. Experimental setup. A photon pair hyperentangled in time-bin and frequency is generated using an unbalanced Michelson interferometer and spontaneous parametric down-conversion (SPDC). Signal and idler photons are sent to Alice and Bob, respectively. Signal photons travel through a 40 km deployed fiber with a total loss of 23.04 dB. White noise is introduced by a co-propagating broadband ASE source. The frequency-resolving module maps frequency modes to time delays via demultiplexing. FBS, fiber beam splitter; SHG, second-harmonic generation; PM, phase modulator; VDL, variable delay line; FPS, fiber phase shifter; EPC, polarization controller; DEMUX, demultiplexer; and MUX, multiplexer.

hyperentangled state, defined over these two degrees of freedom, is described as

$$\frac{1}{\sqrt{2}}\left(|EE\rangle + e^{i\phi_p}|LL\rangle\right) \otimes \int d\omega_s d\omega_i f(\omega_s, \omega_i) |\omega_s, \omega_i\rangle, \tag{6}$$

where ϕ_p is the relative phase determined by the path-length difference in the UMI, and $f(\omega_s, \omega_i)$ denotes the joint spectral amplitude of the two-photon state.

Following quantum state preparation, the hyperentangled photon pair is divided into separate paths by a coarse wavelength-division multiplexing (CWDM) filter with a cutoff wavelength of 1552.52 nm. The signal photon, with a shorter wavelength, is routed to Alice, while the idler photon, with a longer wavelength, is directed to Bob. The signal photon propagates through the deployed fiber channel and is reflected by an FM at the end of the link, resulting in a total path length of 40 km and a channel loss of 23.04 dB. Due to this round-trip transmission, the signal photon acquires an additional time-of-flight of 196 µs relative to the idler photon. To emulate realistic noisy conditions and control the noise portion p in Eq. (4), broadband light from an amplified spontaneous emission (ASE) source is injected into the deployed fiber to co-propagate with the signal photon, introducing tunable white noise.

After distributing the hyperentangled photon pair, the measurement basis for the time-bin state is set by controlling the phases of the unbalanced Mach–Zehnder interferometers (UMZIs) for Alice and Bob, denoted ϕ_A and ϕ_B [2,39]. The UMZIs have a 15 ns path-length difference, matched to that of the initial UMI using a variable delay line (VDL), and are phase-locked using the same stabilization technique. After passing through the UMZIs, the photons undergo frequency-to-time mapping via frequency-resolving modules, implemented as follows. Each module employs a demultiplexer (DEMUX) composed of 12 DWDM filters that resolve the broadband spectrum into individual frequency channels: channels 35–46 for Alice and 16–27 for Bob [50–52]. Channel pairing is based on the frequency anticorrelation of the SPDC source: (35, 27), (36, 26), (37, 25), ..., (46, 16), where channel numbers follow the ITU DWDM grid specification (100 GHz spacing in the telecom C-band). The hyperentangled state in Eq. (6) is thereby projected into

$$\frac{1}{\sqrt{2}}\left(|EE\rangle + e^{i\phi_p}|LL\rangle\right) \otimes \frac{1}{\sqrt{N}} \sum_{n=1}^{N} |n, N+1-n\rangle, \tag{7}$$

where n and $N+1-n$ correspond to frequency modes n_A and n_B in Eq. (4), reflecting the frequency anticorrelation.

To complete the frequency-to-time mapping, a relative temporal delay is introduced by varying the fiber lengths connected to each channel. The delay between adjacent channels is set to 1 ns at the output of the resolving module. For Alice's module, the physical delay is set to 1.5 ns to compensate for the chromatic dispersion induced by the deployed fiber, which reduces the effective temporal spacing by 0.5 ns. For Bob's module, where the idler photon is received directly, the channel delay is set to 1 ns. The relative temporal delays were calibrated by adjusting the fiber lengths through fusion splicing, which can be replaced by programmable VDLs for varying link lengths. All frequency channels are then recombined using a DWDM multiplexer (MUX), resulting in distinct arrival times for each frequency mode. Finally, the photons are detected by superconducting nanowire single-photon detectors (SNSPDs) (Opus One; Quantum Opus), and the arrival times, referenced to the pulsed laser clock, are recorded by a time-tagger (quTAG MC; qutools).

Using the photon arrival time information, the corresponding frequency modes of the detected photons can be inferred, allowing the construction of a 12 × 12 coincidence matrix (for $N = 12$) as shown in Fig. 1(b). Each element of this matrix represents the coincidence count between a pair of frequency modes. By isolating the 12 diagonal elements—where frequency-anticorrelated photon pairs are expected—the contributions from uncorrelated noise, which predominantly populate the off-diagonal elements, are effectively suppressed. To explore the impact of frequency resolution, subsets of the full 12 × 12 matrix are formed by grouping adjacent elements into coarse-grained matrices of size 1 × 1, 2 × 2, 3 × 3, 4 × 4, and 6 × 6. Quantum state tomography (QST) is then performed for each case ($N = 1$, 2, 3, 4, 6, and 12) by modulating the phases of the UMZIs, enabling reconstruction of the density matrix and calculation of the SNR [53,54].

3. RESULTS

Figure 3 shows the measured SNR for time-bin entanglement distributed over the 40 km deployed fiber using frequency-resolved detection. Two cases are analyzed: one without the external noise source ($p = 0.653 \pm 0.023$) and one with additional broadband noise ($p = 0.786 \pm 0.018$). Notably, even in the absence of an external noise source, the noise contribution is non-negligible due to the substantial transmission loss in the deployed fiber (−23.04 dB). This high loss increases vulnerability to uncorrelated noise contributions such as auxiliary laser leakage and detector dark counts. For SNR evaluation, only the computational basis states $|EE\rangle$ and $|LL\rangle$ are considered. The signal is determined from the frequency-anticorrelated coincidence counts after subtracting uncorrelated coincidences, while the noise is estimated from uncorrelated coincidences—including multi-pair emissions, white noise, and detector dark counts (see Supplement 1). A clear improvement in SNR is observed as the number of frequency-resolving modes N increases. For $p = 0.653$, the SNR increases

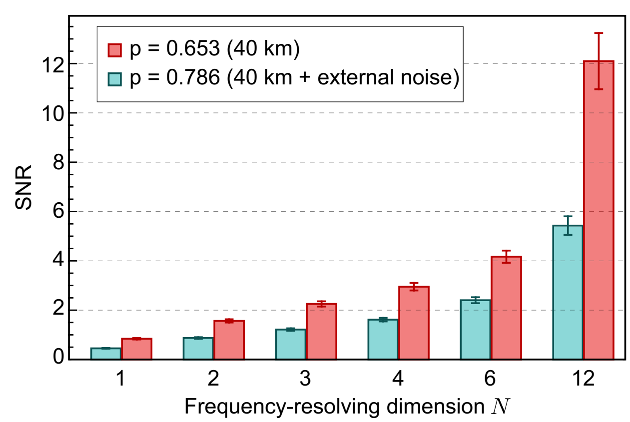

Fig. 3. Signal-to-noise ratio (SNR) of the distributed time-bin state over the 40 km deployed fiber as a function of the number of frequency-resolving modes N. Red and blue bars indicate measured SNRs for noise portions $p = 0.653$ and $p = 0.786$, respectively. As N increases, the SNR improves significantly in both cases, reflecting enhanced discrimination between the entangled photons and uncorrelated noise. Error bars represent one standard deviation, assuming Poissonian photon count statistics.

from 0.84 ± 0.03 at $N = 1$ to 12.10 ± 1.14 at $N = 12$, corresponding to a 14-fold enhancement. Even under stronger noise conditions ($p = 0.786$), the SNR improves from 0.45 ± 0.01 to 5.43 ± 0.38, showing a 12-fold gain. These results highlight the effectiveness of frequency-resolved detection in suppressing noise and preserving entanglement. The values of p are obtained by minimizing the average trace distance between the theoretical density matrix in Eq. (4) and experimentally reconstructed states across all N.

To further assess the impact of frequency-resolved detection, we reconstructed the density matrix ρ of the time-bin entangled state after transmission through the 40 km deployed fiber. Figures 4(a) and 4(b) show the reconstructed density matrices for noise portion $p = 0.653$, without ($N = 1$) and with ($N = 12$) frequency-resolved detection. The fidelity of the distributed time-bin state with respect to the ideal Bell state $|\phi^+\rangle$ is calculated as $\mathcal{F}(\rho) = \langle\phi^+|\rho|\phi^+\rangle$, where ρ is the experimentally reconstructed density matrix. The Bell state fidelity is significantly improved with frequency resolution, indicating that the distributed two-photon state more closely resembles the ideal Bell state. Similarly, Figs. 4(c) and 4(d) show the results for a higher noise portion ($p = 0.786$), where an external noise source is introduced. Again, frequency-resolved detection substantially enhances the fidelity, confirming its robustness against entanglement degradation across varying noise conditions.

We now discuss the impact of frequency-resolved detection on the distribution of entanglement between Alice and Bob through a depolarizing channel, as the noise portion p and the number of frequency-resolved modes N are varied. Figure 5(a) shows the concurrence $C(\rho)$ of the distributed time-bin state, where $C(\rho) = \max(0, \lambda_1 - \lambda_2 - \lambda_3 - \lambda_4)$ and $\lambda_1, \ldots, \lambda_4$ are the eigenvalues, in decreasing order, of the Hermitian matrix $\sqrt{\sqrt{\rho}\tilde{\rho}\sqrt{\rho}}$ [55,56]. For $N = 1$ and $p = 0.786$, the concurrence vanishes, indicating the occurrence of entanglement sudden death (ESD) and rendering the state unusable for quantum communication [57–59]. However, as N increases, the concurrence revives, reaching 0.59 ± 0.09 at $N = 12$. These results confirm that, even under noise conditions severe enough to erase entanglement using conventional detection, the use of hyperentanglement and frequency-resolved detection enables the successful distribution of entanglement across long-distance deployed fiber.

Figure 5(b) shows the Clauser–Horne–Shimony–Holt (CHSH) S parameter [60] for time-bin entanglement distributed over a 40 km deployed fiber with a noise portion of $p = 0.653$. For $N \leq 4$, the S parameter remains below the classical bound of 2, indicating the absence of observable nonlocal correlations and the infeasibility of secure quantum communication. As N increases, however, the S parameter gets improved steadily, demonstrating the recovery of nonlocality—a critical resource for entanglement-based QKD. At $N = 12$, we observe an S parameter of 2.39 ± 0.12, exceeding the CHSH threshold by 3.53 standard deviations. This violation clearly demonstrates that frequency-resolved detection enables the recovery of quantum correlations necessary for secure QKD, even under significant noise and loss conditions.

To evaluate the practical applicability of our method for entanglement-based QKD, we estimated the quantum bit error rate (QBER) and the asymptotic secure key rate R_s derived for coherent attacks. The secure key rate is given by [50,61,62]

$$R_s \geq q\, Q \left\{1 - f(\delta_b) H(\delta_b) - H(\delta_p)\right\}, \tag{8}$$

where q is the basis reconciliation factor (1/4 for the Ekert protocol), Q is the overall gain derived from the experimental joint-detection counts, δ_b and δ_p are the bit and phase error rates, respectively, $f(\delta_b)$ is the error correction efficiency, and $H(x) = -x \log_2(x) - (1 - x) \log_2(1 - x)$ is the binary entropy function. Assuming $f(\delta_b) = 1$ and $\delta_b = \delta_p = \mathcal{E}$, where the QBER $\mathcal{E} = (1 - V)/2$ is evaluated from the two-photon interference visibility V, we observe that our frequency-resolved detection significantly suppresses QBER. For a noise portion of $p = 0.653$ at 40 km, the QBER decreases from 27.64% at $N = 1$ to 7.34% at $N = 12$. At low frequency-resolving dimensions ($N \leq 4$), the estimated secure key rate remains zero due to high loss and noise. However, for $N = 6$ and $N = 12$, the system overcomes

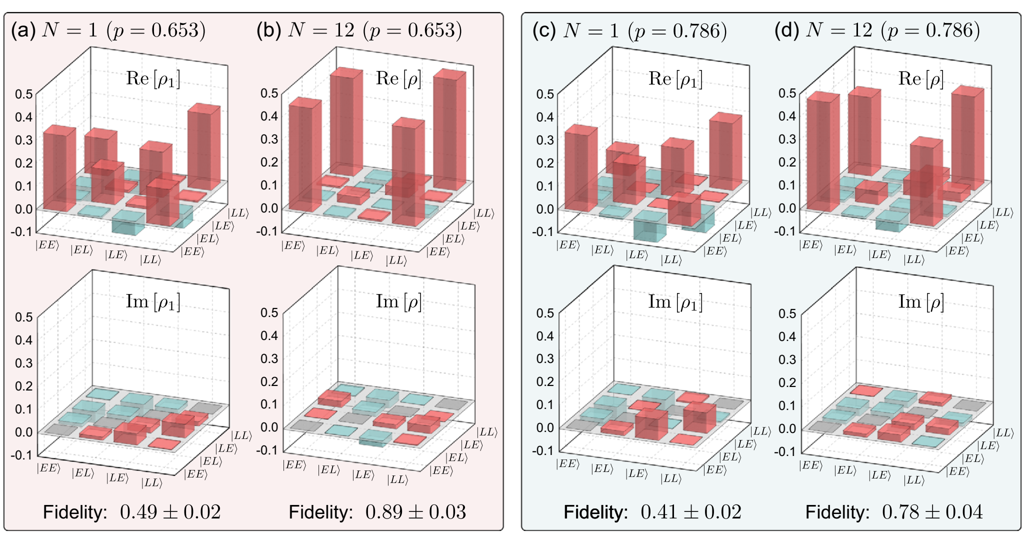

Fig. 4. Reconstructed density matrices of the distributed time-bin entangled state over the 40 km deployed fiber for different numbers of frequency-resolving modes N. For the noise portion $p = 0.653$, the Bell state fidelity improves as N increases from (a) $N = 1$ to (b) $N = 12$, indicating that the distributed two-photon state approaches the ideal Bell state. Even under stronger noise ($p = 0.786$), fidelity is significantly enhanced with increasing N, as shown from (c) $N = 1$ to (d) $N = 12$, demonstrating the effectiveness of frequency-resolved detection in mitigating entanglement degradation. Fidelity errors represent one standard deviation, estimated via a Monte Carlo method with 100 iterations.

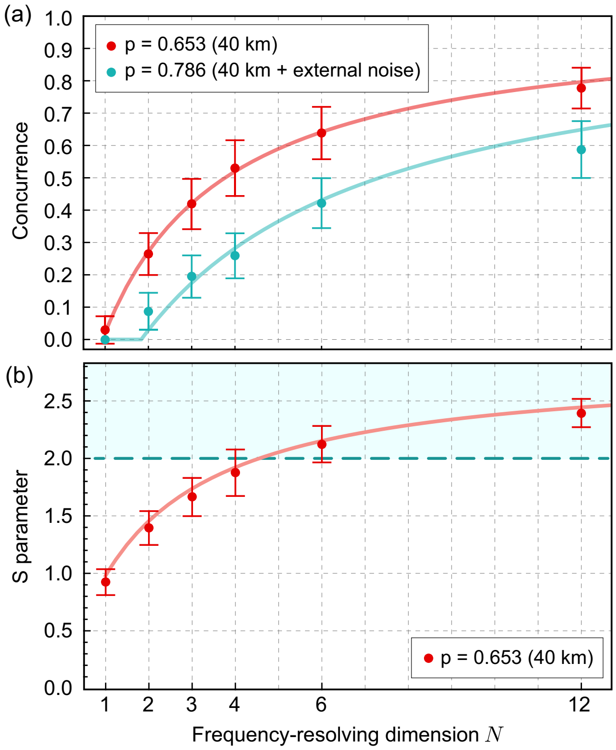

Fig. 5. Concurrence and Clauser–Horne–Shimony–Holt (CHSH) S-parameter of the time-bin entangled state distributed over the 40 km deployed fiber. (a) At $N = 1$ and $p = 0.786$, the concurrence drops to zero, indicating entanglement sudden death (ESD). As N increases, the concurrence is gradually restored, demonstrating the recovery of entanglement enabled by frequency-resolved detection. (b) For $p = 0.653$, the S-parameter increases with N, reaching 2.39 ± 0.12 at $N = 12$, thereby violating the CHSH inequality by 3.53 standard deviations. Error bars indicate one standard deviation, estimated via Monte Carlo simulation with 100 iterations. The solid lines represent the theoretical curves obtained from ρ in Eq. (4) with the noise portion p.

the noise threshold to achieve a positive secure key rate $R_s > 0$, which is consistent with the observation of a CHSH inequality violation ($S > 2$) at these frequency-resolved dimensions (see Supplement 1). Notably, this secure key rate is approximately 10.17 times higher than that of a system using a single conventional 100 GHz DWDM filter. By effectively overcoming severe noise without sacrificing the key generation rate, our approach demonstrates its practical advantage for QKD in real-world fiber networks.

4. CONCLUSION

In conclusion, we have demonstrated a noise-resilient quantum communication protocol that exploits time-bin and frequency hyperentanglement over a 40 km intra-city fiber network with a total channel loss of 23.04 dB. By implementing frequency-resolved detection, our approach effectively suppresses uncorrelated noise, resulting in substantial improvements in both the SNR and Bell-state fidelity of the distributed time-bin entangled state. For a noise portion of $p = 0.653$, the SNR increased by more than a factor of 14, from 0.84 ± 0.03 at $N = 1$ to 12.10 ± 1.14 at $N = 12$, while the Bell-state fidelity improved from 0.49 ± 0.02 to 0.89 ± 0.03, confirming the effectiveness of our method in realistic fiber environments. Furthermore, for a stronger noise portion of $p = 0.786$, the concurrence, which initially dropped to zero due to entanglement sudden death (ESD) at $N = 1$, was revived to 0.59 ± 0.09 at $N = 12$. We also observed a CHSH S-parameter of 2.39 ± 0.12 at $N = 12$ for $p = 0.653$, corresponding to a violation of the CHSH inequality by 3.53 standard deviations. These results demonstrate that entanglement distribution remains viable even under high-loss and high-noise conditions, marking a significant advance toward practical entanglement-based quantum communication over existing optical fiber infrastructure. We anticipate that our approach will contribute to the development of scalable metropolitan quantum networks.

Funding. National Research Foundation of Korea (RS-2023-00208500); Institute of Information & Communications Technology Planning & Evaluation (IITP) (RS-2025-02263264); Information Technology Research Center support program (IITP-2025-RS-2022-00164799); National Research Council of Science and Technology (CAP22053-000).

Acknowledgment. The authors thank the KRISS Time & Frequency Group for the help with fiber link preparation, and KISTI for their support through the KREONET advanced research program.

Disclosures. The authors declare no conflicts of interest.

Data availability. Data underlying the results presented in this paper are not publicly available at this time but may be obtained from the authors upon reasonable request.

Supplemental document. See Supplement 1 for supporting content.

REFERENCES

1. A. K. Ekert, "Quantum cryptography based on Bell's theorem," Phys. Rev. Lett. **67**, 661–663 (1991).
2. J. D. Franson, "Bell inequality for position and time," Phys. Rev. Lett. **62**, 2205–2208 (1989).
3. W. Tittel, J. Brendel, H. Zbinden, *et al.*, "Quantum cryptography using entangled photons in energy-time Bell states," Phys. Rev. Lett. **84**, 4737–4740 (2000).
4. C. H. Bennett, G. Brassard, and N. D. Mermin, "Quantum cryptography without Bell's theorem," Phys. Rev. Lett. **68**, 557–559 (1992).
5. D. S. Naik, C. G. Peterson, A. G. White, *et al.*, "Entangled state quantum cryptography: eavesdropping on the Ekert protocol," Phys. Rev. Lett. **84**, 4733–4736 (2000).
6. T. Jennewein, C. Simon, G. Weihs, *et al.*, "Quantum cryptography with entangled photons," Phys. Rev. Lett. **84**, 4729–4732 (2000).
7. J. Yin, Y.-H. Li, S.-K. Liao, *et al.*, "Entanglement-based secure quantum cryptography over 1,120 kilometres," Nature **582**, 501–505 (2020).
8. D. Bouwmeester, J.-W. Pan, K. Mattle, *et al.*, "Experimental quantum teleportation," Nature **390**, 575–579 (1997).
9. D. Boschi, S. Branca, F. De, *et al.*, "Experimental realization of teleporting an unknown pure quantum state via dual classical and Einstein-Podolsky-Rosen channels," Phys. Rev. Lett. **80**, 1121–1125 (1998).
10. A. Furusawa, J. L. Sørensen, S. L. Braunstein, *et al.*, "Unconditional quantum teleportation," Science **282**, 706–709 (1998).
11. Y.-H. Kim, S. P. Kulik, and Y. Shih, "Quantum teleportation of a polarization state with a complete Bell state measurement," Phys. Rev. Lett. **86**, 1370–1373 (2001).
12. I. Marcikic, H. De Riedmatten, W. Tittel, *et al.*, "Long-distance teleportation of qubits at telecommunication wavelengths," Nature **421**, 509–513 (2003).
13. J.-G. Ren, P. Xu, H.-L. Yong, *et al.*, "Ground-to-satellite quantum teleportation," Nature **549**, 70–73 (2017).
14. D.-G. Im, C.-H. Lee, Y. Kim, *et al.*, "Optimal teleportation via noisy quantum channels without additional qubit resources," npj Quantum Inf. **7**, 86 (2021).
15. C. H. Bennett and S. J. Wiesner, "Communication via one- and two-particle operators on Einstein-Podolsky-Rosen states," Phys. Rev. Lett. **69**, 2881–2884 (1992).

16. K. Mattle, H. Weinfurter, P. G. Kwiat, *et al.*, "Dense coding in experimental quantum communication," Phys. Rev. Lett. **76**, 4656–4659 (1996).
17. Y.-H. Kim, "Single-photon two-qubit entangled states: preparation and measurement," Phys. Rev. A **67**, 040301R (2003).
18. J. T. Barreiro, T.-C. Wei, and P. G. Kwiat, "Beating the channel capacity limit for linear photonic superdense coding," Nat. Phys. **4**, 282–286 (2008).
19. B. P. Williams, R. J. Sadlier, and T. S. Humble, "Superdense coding over optical fiber links with complete Bell-state measurements," Phys. Rev. Lett. **118**, 050501 (2017).
20. H. J. Kimble, "The quantum internet," Nature **453**, 1023–1030 (2008).
21. S. K. Joshi, D. Aktas, S. Wengerowsky, *et al.*, "A trusted node–free eight-user metropolitan quantum communication network," Sci. Adv. **6**, eaba0959 (2020).
22. L.-J. Wang, K.-H. Zou, W. Sun, *et al.*, "Long-distance copropagation of quantum key distribution and terabit classical optical data channels," Phys. Rev. A **95**, 012301 (2017).
23. A. N. Craddock, A. Lazenby, G. B. Portmann, *et al.*, "Automated distribution of polarization-entangled photons using deployed New York City fibers," PRX Quantum **5**, 030330 (2024).
24. J. M. Thomas, F. I. Yeh, J. H. Chen, *et al.*, "Quantum teleportation coexisting with classical communications in optical fiber," Optica **11**, 1700–1707 (2024).
25. S. P. Neumann, A. Buchner, L. Bulla, *et al.*, "Continuous entanglement distribution over a transnational 248 km fiber link," Nat. Commun. **13**, 6134 (2022).
26. Y.-C. Jeong, Y.-S. Kim, and Y.-H. Kim, "Effects of depolarizing quantum channels on BB84 and SARG04 quantum cryptography protocols," Laser Phys. **21**, 1438–1442 (2011).
27. H. Yu, S. Sciara, M. Chemnitz, *et al.*, "Quantum key distribution implemented with *d*-level time-bin entangled photons," Nat. Commun. **16**, 171 (2025).
28. S. Ecker, F. Bouchard, L. Bulla, *et al.*, "Overcoming noise in entanglement distribution," Phys. Rev. X **9**, 041042 (2019).
29. Z.-Q. Zhong, X.-H. Zhan, J.-L. Chen, *et al.*, "Hyperentanglement quantum communication over a 50 km noisy fiber channel," Optica **11**, 1056–1061 (2024).
30. M. Zahidy, D. Ribezzo, C. De, *et al.*, "Practical high-dimensional quantum key distribution protocol over deployed multicore fiber," Nat. Commun. **15**, 1651 (2024).
31. J. M. Thomas, G. S. Kanter, and P. Kumar, "Designing noise-robust quantum networks coexisting in the classical fiber infrastructure," Opt. Express **31**, 43035–43047 (2023).
32. F. Zhu, M. Tyler, N. H. Valencia, *et al.*, "Is high-dimensional photonic entanglement robust to noise?" AVS Quantum Sci. **3**, 011401 (2021).
33. X.-H. Li and S. Ghose, "Hyperentanglement concentration for time-bin and polarization hyperentangled photons," Phys. Rev. A **91**, 062302 (2015).
34. T.-M. Zhao, Y. S. Ihn, and Y.-H. Kim, "Direct generation of narrow-band hyperentangled photons," Phys. Rev. Lett. **122**, 123607 (2019).
35. J.-H. Kim, Y. Kim, D.-G. Im, *et al.*, "Noise-resistant quantum communications using hyperentanglement," Optica **8**, 1524–1531 (2021).
36. J. C. Chapman, C. C. W. Lim, and P. G. Kwiat, "Hyperentangled time-bin and polarization quantum key distribution," Phys. Rev. Appl. **18**, 044027 (2022).
37. A. Mueller, S. I. Davis, B. Korzh, *et al.*, "High-rate multiplexed entanglement source based on time-bin qubits for advanced quantum networks," Opt. Quantum **2**, 64–71 (2024).
38. I. Marcikic, H. De Riedmatten, W. Tittel, *et al.*, "Time-bin entangled qubits for quantum communication created by femtosecond pulses," Phys. Rev. A **66**, 062308 (2002).
39. I. Marcikic, H. De Riedmatten, W. Tittel, *et al.*, "Distribution of time-bin entangled qubits over 50 km of optical fiber," Phys. Rev. Lett. **93**, 180502 (2004).
40. C. H. Bennett, P. W. Shor, J. A. Smolin, *et al.*, "Entanglement-assisted classical capacity of noisy quantum channels," Phys. Rev. Lett. **83**, 3081 (1999).
41. Y.-C. Jeong, J.-C. Lee, and Y.-H. Kim, "Experimental implementation of a fully controllable depolarizing quantum operation," Phys. Rev. A **87**, 014301 (2013).
42. R. F. Werner, "Quantum states with Einstein-Podolsky-Rosen correlations admitting a hidden-variable model," Phys. Rev. A **40**, 4277–4281 (1989).
43. Y.-S. Zhang, Y.-F. Huang, C.-F. Li, *et al.*, "Experimental preparation of the Werner state via spontaneous parametric down-conversion," Phys. Rev. A **66**, 062315 (2002).
44. Y.-H. Kim and W. P. Grice, "Measurement of the spectral properties of the two-photon state generated via type II spontaneous parametric down-conversion," Opt. Lett. **30**, 908–910 (2005).
45. S.-Y. Baek and Y.-H. Kim, "Spectral properties of entangled photon pairs generated via frequency-degenerate type-I spontaneous parametric down-conversion," Phys. Rev. A **77**, 043807 (2009).
46. K.-K. Park, J.-H. Kim, T.-M. Zhao, *et al.*, "Measuring the frequency-time two-photon wavefunction of narrowband entangled photons from cold atoms via stimulated emission," Optica **4**, 1293–1297 (2017).
47. Y.-W. Cho, K.-K. Park, J.-C. Lee, *et al.*, "Engineering frequency-time quantum correlation of narrow-band biphotons from cold atoms," Phys. Rev. Lett. **113**, 063602 (2014).
48. S.-Y. Baek, Y.-W. Cho, and Y.-H. Kim, "Nonlocal dispersion cancellation using entangled photons," Opt. Express **17**, 19241–19252 (2009).
49. S.-Y. Baek, O. Kwon, and Y.-H. Kim, "Nonlocal dispersion control of a single-photon waveform," Phys. Rev. A **78**, 013816 (2008).
50. J.-H. Kim, J.-W. Chae, Y.-C. Jeong, *et al.*, "Quantum communication with time-bin entanglement over a wavelength-multiplexed fiber network," APL Photonics **7**, 016106 (2022).
51. J.-W. Chae, H. Seo, and Y.-H. Kim, "DWDM-based effective group velocity dispersion module for long-distance quantum communication," J. Lightwave Technol. **43**, 81–86 (2025).
52. J.-W. Chae, H. Seo, U.-S. Kim, *et al.*, "Verifying energy-time entanglement via nonlocal dispersion cancellation," Phys. Rev. A **111**, L030403 (2025).
53. D. F. V. James, P. G. Kwiat, W. J. Munro, *et al.*, "Measurement of qubits," Phys. Rev. A **64**, 052312 (2001).
54. H. Takesue and Y. Noguchi, "Implementation of quantum state tomography for time-bin entangled photon pairs," Opt. Express **17**, 10976–10989 (2009).
55. W. K. Wootters, "Entanglement of formation of an arbitrary state of two qubits," Phys. Rev. Lett. **80**, 2245–2248 (1998).
56. D.-G. Im and Y.-H. Kim, "Decoherence-induced sudden death of entanglement and Bell Nonlocality," Photonics **9**, 58 (2022).
57. M. P. Almeida, F. de Melo, M. Hor-Meyll, *et al.*, "Environment-induced sudden death of entanglement," Science **316**, 579–582 (2007).
58. Y.-S. Kim, J.-C. Lee, O. Kwon, *et al.*, "Protecting entanglement from decoherence using weak measurement and quantum measurement reversal," Nat. Phys. **8**, 117–120 (2012).
59. H.-T. Lim, J.-C. Lee, K.-H. Hong, *et al.*, "Avoiding entanglement sudden death using single-qubit quantum measurement reversal," Opt. Express **22**, 19055–19068 (2014).
60. J. F. Clauser, M. A. Horne, A. Shimony, *et al.*, "Proposed experiment to test local hidden-variable theories," Phys. Rev. Lett. **23**, 880–884 (1969).
61. M. Koashi and J. Preskill, "Secure quantum key distribution with an uncharacterized source," Phys. Rev. Lett. **90**, 057902 (2003).
62. X. Ma, C.-H. F. Fung, and H.-K. Lo, "Quantum key distribution with entangled photon sources," Phys. Rev. A **76**, 012307 (2007).